
ASSESSMENT OF ZONALLY SYMMETRIC AND ASYMMETRIC COMPONENTS OF THE SOUTHERN ANNULAR MODE USING A NOVEL APPROACH

A PREPRINT

Elio Campitelli
UBA - FCEN - DCAO

Leandro Díaz
UBA - FCEN - DCAO

Carolina Vera
UBA - FCEN - DCAO

`elio.campitelli@cima.fcen.uba.ar`

December 16, 2020

Abstract

The Southern Annular Mode (SAM) is the main mode of variability in the Southern Hemisphere extra-tropical circulation and it is so called because of its zonally symmetric ring-like shape. However, the SAM pattern actually contains noticeable deviations from zonal symmetry. Thus, the purpose of this study is to describe the zonally asymmetric and symmetric components of the SAM variability and their impacts. We regress monthly geopotential height fields at each level onto the asymmetric and symmetric component of the SAM to create two new indices: Asymmetric SAM (A-SAM) and Symmetric SAM (S-SAM). In the troposphere, the A-SAM is associated with a zonal wave 3 which is rotated a quarter wavelength with respect to the climatological zonal wave 3, is much stronger in the Pacific ocean, where it extends vertically to the stratosphere with an equivalent barotropic structure. On the other hand, the S-SAM is associated with negative geopotential height anomalies over Antarctica surrounded by a zonally symmetric ring of positive geopotential height anomalies. The observed relationship between the El Niño Southern Oscillation and the SAM is fully explained by the A-SAM index. The positive trend of the SAM is present only in its symmetric component. Despite this, the SAM is becoming more zonally asymmetric. The regional impacts of the SAM in temperature and precipitation are strongly affected by its asymmetric component.

Keywords Southern Annular Mode · general circulation · zonally asymmetric circulation · El Niño Southern Oscillation

1 Introduction

The Southern Annular Mode (SAM) is the main mode of variability in the Southern Hemisphere extratropical circulation (Rogers and van Loon, 1982) on daily, monthly, and decadal timescales (Baldwin, 2001; Fogt and Bromwich, 2006) and exerts an important influence on temperature and precipitation anomalies, and sea ice concentration (e.g. Fogt and Marshall, 2020). Its positive phase is usually described as anomalously low pressures over Antarctica surrounded by a ring of anomalous high pressures in middle-to-high latitudes.

Most authors describe the SAM as a zonally symmetric pattern, a fact that is reflected not only in its name, but also in the various methods used to characterise it. Of the several different indices presented in the literature, many of them are based on zonal means of sea level pressure or geopotential height (Ho et al., 2012). Gong and Wang (1999) defined the SAM index as the zonal mean sea level pressure difference between 40°S and 60°S, which is also the definition used by the station-based index in Marshall (2003). Baldwin and Thompson (2009) proposed defining the Northern and Annular modes as the leading EOF of the zonally averaged geopotential height at each level.

Even though these indices are based on zonal averages, their associated geopotential height spatial anomalies contain noticeable deviations from zonal symmetry, particularly in the Pacific Ocean region. The zonal asymmetries have not been widely studied, but previous work suggest that they strongly modulate the regional impacts of the SAM (Fan, 2007; Silvestri and Vera, 2009; Fogt et al., 2012; Rosso et al., 2018). The fact that the SAM is not entirely zonally symmetric hinders our ability to reconstruct its historical variability prior to the availability of dense observations in the Southern Hemisphere (Jones et al., 2009).

Some of the variability associated with the zonal asymmetries of the SAM seems to be forced by the tropics. ENSO-like variability affects the Southern Hemisphere extratropics through the Rossby wave trains (Mo and Ghil, 1987; Kidson, 1988; Karoly, 1989) which project strongly onto the zonal anomalies associated with the SAM in the Pacific sector. Moreover, tropical influences on the SAM have been observed (Fan, 2007; Fogt et al., 2011; Clem and Fogt, 2013). Fan (2007) computed SAM indices of the Western and the Eastern Hemispheres separately and found that they were much more correlated to each other if the (linear) signal of the ENSO was removed.

Positive trends in the SAM have been documented by various researchers using different indices, mostly on austral Summer and Autumn (e.g. Fogt and Marshall, 2020, and references therein). It is thought that these trends are driven primarily by stratospheric ozone depletion and the increase in greenhouse gases, and understood in the context of zonal mean variables (Marshall et al., 2004; Gillett et al., 2005; Arblaster and Meehl, 2006; Gillett et al., 2013). However, it's not clear yet how or if the asymmetric SAM component responds to these forcings, or how its variability alters the observed trends.

The impact of the zonally asymmetric component of the SAM at regional scales has not been studied in detail yet. The positive phase of the SAM is associated with colder-than-normal temperatures over Antarctica and warmer-than-normal temperatures at higher latitudes (Jones et al., 2019) (and vice versa for negative SAM). But there are significant deviations from this zonal mean response, notably in the Antarctic Peninsula and the South Atlantic (Fogt et al., 2012). The SAM-related signal on precipitation anomalies behaves similarly, although with even greater deviation from zonal symmetry (Lim et al., 2016). The importance of zonal asymmetries of the SAM on these impacts have been studied in certain regions. For example, the SAM-precipitation relationship in Southeastern South America can be explained by the Pacific-South American (PSA)-like zonally asymmetric circulation associated with the SAM (Silvestri and Vera, 2009; Rosso et al., 2018). Fan (2007) also found that precipitation in East Asia was impacted by the variability of only the Western Hemisphere part of the SAM.

The study of the temporal variability of the asymmetric component of the SAM has not received much attention except for Fogt et al. (2012). This study provides evidences for the relevance of the SAM's asymmetric component. However, their conclusions are based on composites of positive and negative SAM events including a small number of cases unevenly distributed among years with and without satellite information. The latter is particularly important due to the inhomogeneities in reanalysis products prior to the satellite era and the possible change in the asymmetric structure of the SAM (Silvestri and Vera, 2009). Moreover, Fogt et al. (2012) studied the zonal asymmetric component of the SAM only in sea level pressure. Zonal asymmetries in the SAM spatial pattern are fairly barotropic throughout the troposphere, but they change dramatically in the stratosphere (Baldwin and Thompson, 2009).

Our objective is, then, to describe the zonally asymmetric and symmetric components of the SAM variability. We first propose a methodology that provides for each level, two indices which aim to capture independently the variability of the symmetric and asymmetric SAM component respectively. Their vertical structure and coherence, temporal variability and trends are consequently assessed. We then study the spatial patterns described by the variability exclusive to each index focusing on 50 hPa as representing the stratosphere and 700 hPa as representing the troposphere. Finally, the relationships of the SAM at 700 hPa with temperature and precipitation anomalies are investigated.

In the Section 2 we describe the methods. In Section 3.1 we describe the temporal variability and vertical coherence of the indices. In Section 3.2, we analyse the spatial patterns of geopotential height associated with them. In Section 3.3, we study their relationship with surface-level temperature and precipitation.

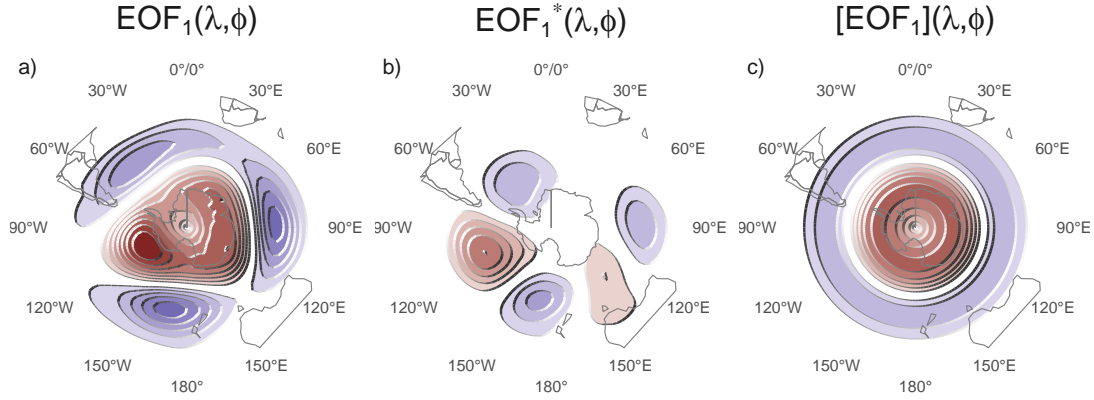


Figure 1: Spatial patterns of the first EOF of 700 hPa geopotential height for 1979 - 2018 period. (a) Full field, (b) zonally asymmetric component and (c) zonally symmetric component. Arbitrary units.

2 Methods

2.1 Data

We used monthly geopotential height at 2.5° longitude by 2.5° latitude of horizontal resolution and 37 vertical isobaric levels from ERA5 (Hersbach et al., 2020) for the period 1979 to 2018. We restrict our analysis to the post-satellite era to avoid any confounding factors arising from the incorporation of satellite observations.

Temperature data used are from NOAA’s Merged Land Ocean Global Surface Temperature Analysis V4.0.1 (Smith et al., 2008; Vose et al., 2012), which blends land surface air temperature and sea surface (water) temperature analysis into a monthly global grid 5° longitude by 5° latitude. Monthly rainfall fields at 0.5° longitude by 0.5° latitude data from the Global Precipitation Climatology Centre (Schneider et al., 2015, 2017) are also considered. The rainfall dataset is based on station-based records, and thus it only has continental coverage.

2.2 Definition of indices

Traditionally, the SAM is defined as the leading empirical orthogonal mode (EOF) of sea-level pressure or geopotential height anomalies at low levels (Ho et al., 2012). Following Baldwin and Dunkerton (2001), we extend that definition vertically and use the term SAM to refer to the leading EOF of the monthly anomalies of geopotential height south of 20°S at each level. We performed EOFs by computing the Singular Value Decomposition of the data matrix consisting in 480 rows and 4176 columns (144 points of longitude and 29 points of latitude). We weighted the values by the square root of the cosine of latitude to account for the non-equal area of each gridpoint (Chung and Nigam, 1999). We consider in the EOF analysis all months together without dividing by seasons.

To separate the zonally symmetric and asymmetric components of the SAM, we computed the zonal mean and anomalies of the full SAM spatial pattern, as shown in Figure 1 at 700 hPa. The full spatial signal ($\text{EOF}_1(\lambda, \phi)$) is the sum of the zonally asymmetric ($\text{EOF}_1^*(\lambda, \phi)$) and symmetric ($[\text{EOF}_1](\lambda, \phi)$) components. We then compute the SAM index, Asymmetric SAM index (A-SAM) and Symmetric SAM (S-SAM) indices as the coefficients of the regression of each monthly geopotential height field on the respective patterns (weighting by the cosine of latitude). The three indices are then normalized by dividing them by the standard deviation of the SAM index at each level. As a result, the magnitudes between indices are comparable. However, only SAM index has unit standard deviation per definition. The explained variance of each pattern is used as an indicator of the degree of zonally symmetry or asymmetry of each monthly field. To quantify the coherence between temporal series corresponding to different indices or the same index at different levels, we computed the temporal correlation between them.

The method assumes linearity in the asymmetric component of the SAM. That means that zonal asymmetries associated with positive SAM phase (SAM+) are almost opposite in sign and of the same magnitude to the

ones associated with negative SAM phase (SAM-). Fogt et al. (2012)’s composites (their Figure 4) suggest that this might not be entirely valid, although much of that apparent non-linearity could be due to the heterogenous nature of the selected years for constructing the composites. To test this assumption, we computed seasonal composites of zonal anomalies of geopotential height for SAM+ and SAM- (defined as months in which the SAM index is greater than 1 standard deviation and lower than minus 1 standard deviation, respectively) for the period from 1979 to 2018 at the 700 hPa and 50 hPa levels (Figures A.1 and A.2). In all seasons and both levels, SAM+ composites are similar to SAM- in structure but with the opposite sign. Spatial correlations between composites for each season are high. The method considered in this study seems then a reasonable approximation of the phenomenon.

By performing the EOF analysis using data for all months we are assuming that the zonally asymmetric structure of the SAM is the same at all seasons. The latter was assessed by computing geopotential height zonal anomalies by projecting the first EOF of each season independently. The following seasons were considered – December to February (DJF), March to May (MAM), June to August (JJA) and September to November (SON). Results are very similar to each other in the troposphere (Figure A.3, row 1) and show spatial correlations between 0.65 (DJF with JJA) and 0.9 (MAM with SON). In the stratosphere (Figure A.3, row 2), patterns are similar for all seasons except DJF, when the wave-1 zonal anomalies are rotated 90° in comparison with the rest of the year. Spatial correlations in the stratosphere are between -0.24 (DJF with SON) and 0.95 (MAM with JJA). Therefore, the results confirm that the zonal asymmetric structure of the SAM is very similar throughout most of the year with the exception of DJF in the stratosphere.

The method also assumes that the zonally asymmetric pattern of the SAM remains stationary along the period considered. Silvestri and Vera (2009) suggest that this might not be the case between 1958 and 2004. Zonal asymmetric patterns of SAM were computed for the two halves of the period (1979 to 1998 and 1999 to 2018) respectively. They show no systematic change neither in the stratosphere nor in the troposphere (Figure A.4).

2.3 Regressions

We performed linear regressions to quantify the association between the SAM indices and other variables. Moreover, we apply multiple linear regression analysis to describe the combined influence of both A-SAM and S-SAM. To obtain the linear coefficients of a variable X (geopotential, temperature, precipitation, etc...) with A-SAM and S-SAM we fit the equation

$$X(\lambda, \phi, t) = \alpha(\lambda, \phi) \text{A-SAM} + \beta(\lambda, \phi) \text{S-SAM} + X_0(\lambda, \phi) + \epsilon(\lambda, \phi, t)$$

where λ and ϕ are the longitude and latitude, t is the time, α and β are the linear regression coefficients, X_0 and ϵ are the constant and error terms. From this equation, α represents the (linear) association of X with the variability of A-SAM that is not explained by the variability of S-SAM; i.e. it is proportional to the partial correlation of X and A-SAM, controlling for the effect of S-SAM, and vice versa for β . When performing a separate regression for each trimester (DJF, MAM, JJA, SON), we averaged the relevant variables seasonally for each year and trimester before computing the regression.

Statistical significance for regression fields were evaluated adjusting p-values by controlling for the False Discovery Rate (Benjamini and Hochberg, 1995; Wilks, 2016) to avoid misleading results from the high number of regressions (Walker, 1914; Katz and Brown, 1991).

Linear trends were computed by Ordinary Least Squares and the 95% confidence interval was computed assuming a t-distribution with the appropriate residual degrees of freedom. To the amplitude of the zonal waves is defined through computing the Fourier transform of the spatial field at each latitude circle.

We computed density probability estimates using a Gaussian kernel of optimal bin width according to Sheather and Jones (1991).

2.4 Computation procedures

We performed all analysis in this paper using the R programming language (R Core Team, 2020), using the data.table package (Dowle et al., 2020) and the metR package (Campitelli, 2020). All graphics are made using ggplot2 (Wickham, 2009). We downloaded data from reanalysis using the ecmwfr package (Hufkens et al., 2020) and indices of the ENSO with the rsoi package (Albers and Campitelli, 2020). The paper was rendered using knitr and rmarkdown (Xie, 2015; Allaire et al., 2019).

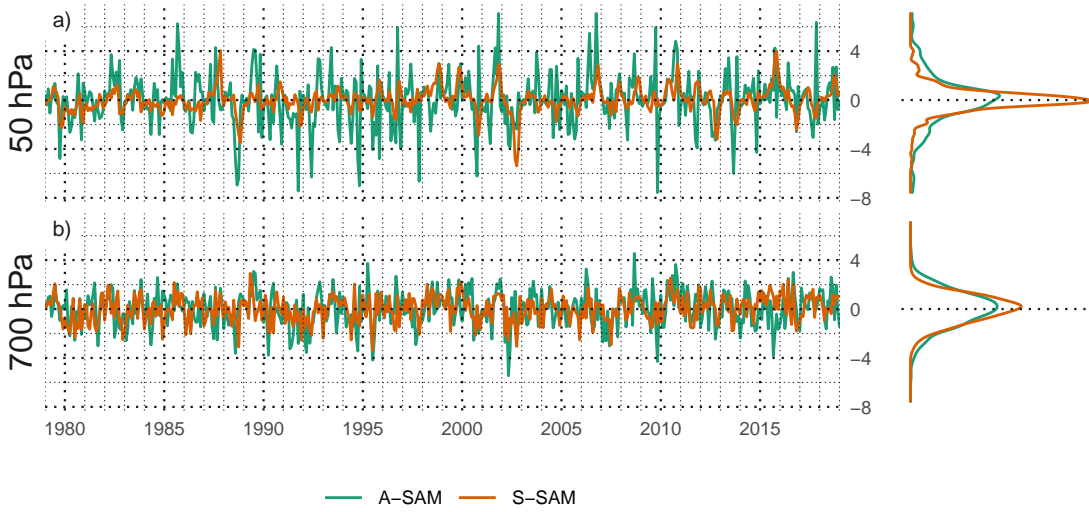


Figure 2: Time series for A-SAM and S-SAM at (a) 50 hPa and (b) 700 hPa. To the right, probability density estimate of each index. Series are standardised by the standard deviation of the SAM at each level.

3 Results

3.1 Temporal evolution

We first assess the temporal evolution of A-SAM and S-SAM. Figure 2 shows the corresponding time series for 700 hPa and 50 hPa and their corresponding density estimates. We selected these two levels as representative of the tropospheric and stratospheric variability respectively. As it is shown below, the variabilities of both indices are highly coherent within each atmospheric layer, therefore it is reasonable to take one level as representative of each layer.

Month-to-month variability is evident for both indices, with noisy variations in the low frequencies. At first glance the series can be distinguished by their distributions. Compared to the tropospheric indices, the stratospheric indices are much more long-tailed; that is, extreme values (both negative and positive) abound. The A-SAM series have both more variability in the higher frequencies than the S-SAM series.

The stratospheric S-SAM varies strongly with a two-year period, which can be seen by spectral analysis (Figure A.6). This might suggest a link between stratospheric SAM variability and the Quasi-Biennial Oscillation (Baldwin et al., 2001). A local peak at 2 years is discernible in the periodogram of the tropospheric S-SAM, although it's not statistically significant. In the troposphere the most significant peak of variability is found in A-SAM at around 3.6 months.

From a visual inspection, the A-SAM and S-SAM time series appear to be correlated. Moreover, looking at the extremes in the stratosphere, the S-SAM series appears to lag the A-SAM series (see, for example, the positive events on late 1987). Figure 3 shows these correlations along all levels considered, for zero and -1 lags. Values of zero-lag correlations between A-SAM and S-SAM are relatively constant throughout the troposphere, fluctuating between 0.39 and 0.45. One-month-lag correlations are similarly constant but significantly reduced to around 0.17. In the stratosphere, zero-lag correlations drop to a minimum of 0.21 at 20 hPa and then increase again monotonically with height up to the uppermost level of the reanalysis (although results near the top of the models are to be interpreted with care). At the same time, one-month-lag correlations increase with height. Therefore, stratospheric A-SAM index tends to precede the S-SAM index. (Correlations at lags -5 to 5 are shown in Figure A.5.)

Figure 4 shows (zero-lag) cross-correlation across levels for the SAM, A-SAM and S-SAM indices. For the SAM (Figure 4a), high values below 100 hPa reflect the vertical (zero-lag) coherency throughout the troposphere. Above 100 hPa, correlation between levels does fall off more rapidly, indicating less coherent (zero-lag) variability. But correlations between tropospheric and lower-to-middle stratospheric levels are still relatively high (e.g. greater than 0.4 between tropospheric levels and levels below 30 hPa). A-SAM and

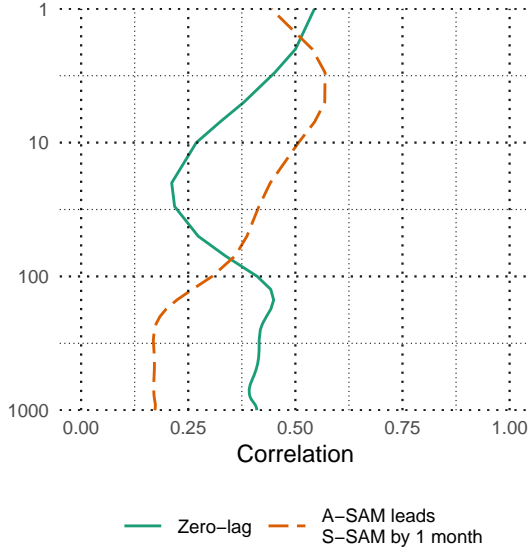


Figure 3: Correlation between S-SAM and A-SAM at each level for lag zero and lag -1 (A-SAM leads S-SAM) for the 1979 – 2018 period.

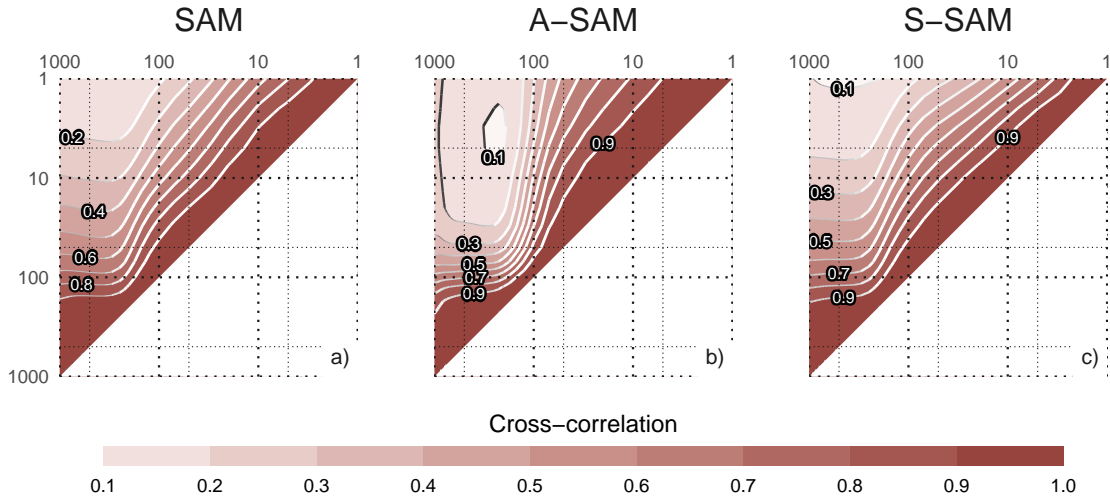


Figure 4: Cross correlation between levels for the (a) SAM, (b) A-SAM, and (c) S-SAM for the 1979 – 2018 period.

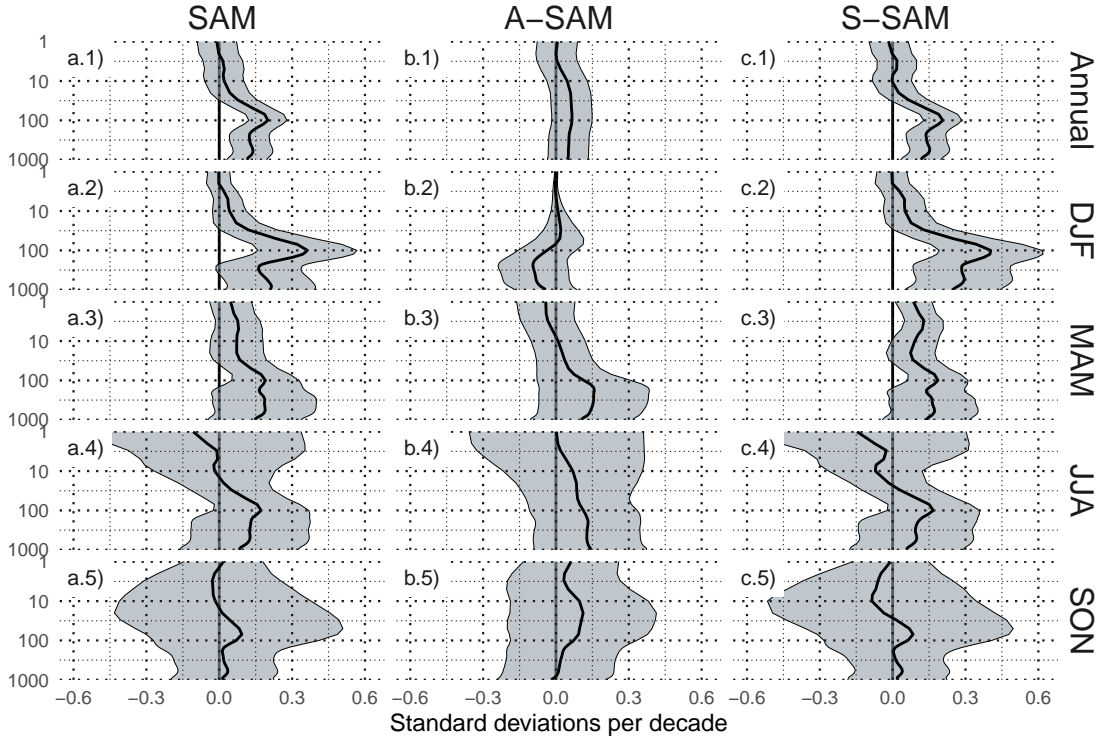


Figure 5: Linear trends (in standard deviations per decade) at each level for annual (row 1) and seasonal values (rows 2 to 5) for the period 1979 – 2018 and for the (column a) SAM index, (column b) A-SAM index, and (column c) S-SAM index. Shading indicates the 95% confidence interval from a t-distribution.

S-SAM (Figure 4b and c, respectively) share similar high level of coherency in the troposphere but they differ in their stratospheric behaviour. Stratospheric coherency is stronger for the A-SAM than the S-SAM. The stratospheric S-SAM seems to connect more strongly to the troposphere than the stratospheric A-SAM.

The linear trends for each of the indices (SAM, S-SAM and A-SAM) were evaluated for the complete period 1979 – 2018 at each level for the whole year and separated by trimesters (Figure 5). The SAM index presents a statistically positive significant trend (Figure 5a.1) that extends throughout the troposphere up to about 50 hPa and reaches its maximum value at 100 hPa. The seasonal trends (rest of Figure 5 column a) indicate that positive trends are present in Autumn and particularly in Summer, where the 100 hPa maximum is much more defined. In Winter and Spring, we detect no statistically significant trend. This is consistent with the results of previous studies, which find large positive trends in Summer, smaller in Autumn and no trends in the other seasons (e.g. Fogt and Marshall, 2020, and references therein) using indices of the SAM based on surface or near-surface circulation.

By separating the SAM signal in its asymmetric and symmetric parts, not only we can see that these trends are almost entirely due to the symmetric component (column b vs. column c in Figure 5), but in some cases the trends become clearer. In Summer, A-SAM has a statistically non significant negative trend in the middle troposphere that obscures the trend in the SAM index; as a result, trends computed using only the Symmetric component are stronger (compare the shading region in Figure 5a.2 and c.2). In Autumn, the S-SAM index reveals a statistically significant positive trend in the stratosphere that is not significant using the SAM index.

Figure 6 shows trends for the explained variance of each index. There is no evidence of a significant trend in the stratosphere. In the troposphere, there is a positive trend for A-SAM and no significant trend for S-SAM. This suggest that the SAM has become more asymmetric in the period from 1979 to 2018. However, the change is slight, around 1% increased explained variance per decade.

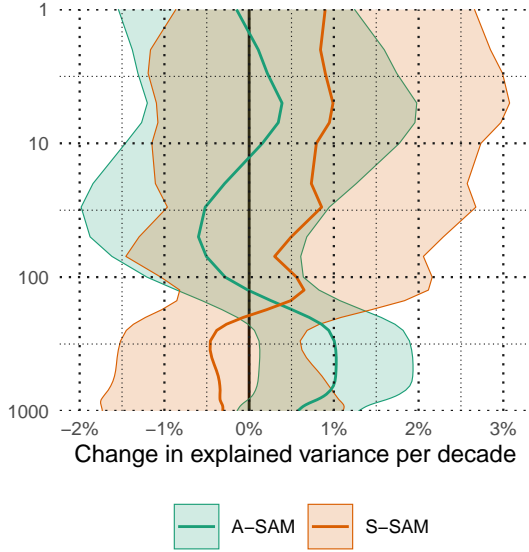


Figure 6: Linear trends (in percent per decade) of the variance explained by A-SAM and S-SAM at each level for the period 1979 – 2018. Shading indicates the 95% confidence interval.

3.2 Spatial patterns

We then computed the spatial regression of geopotential height anomalies on the A-SAM and S-SAM indices at 700 hPa and 50 hPa levels (Figure 7). While regression coefficients in Figure 7 column a are computed using SAM, the regression coefficients in columns b and c of Figure 7 are computed using multiple regression using the A-SAM and S-SAM indices at the same time. Thus, they are to be interpreted as the patterns associated with each index, removing the variability (linearly) explained by the other one.

In the stratosphere, the spatial pattern associated with the SAM is clearly dominated by a zonally symmetric, monopolar structure (Figure 7a.1) which is not centred in the South Pole. On the other hand, the monopole associated with S-SAM (Figure 7c.1) is more symmetric. Furthermore, the regression pattern of A-SAM is characterized by a wave-1 structure with centres over the Bellinghausen Sea on the Western Hemisphere and Davis Sea in the Eastern Hemisphere

In the troposphere, the regression pattern associated with the SAM shows the well-known combination of zonally symmetrical annular mode with zonal asymmetries in the form of a wave-3 (Figure 7a.2, (Fogt et al., 2012)). The regression patterns associated with the A-SAM and S-SAM indices successfully disentangle both structures. While the A-SAM index gives rise to a cleaner zonal wave (Figure 7b.2), the S-SAM index is associated with an annular structure, almost devoid of zonal asymmetries (Figure 7c.2). The wave-3 pattern observed in Figure 7b.2 is rotated by half a wavelength from the average position of the mean wave-3 pattern described by Raphael (2004), whose reference locations are marked with points in the figure. Indeed, there is no correlation between Raphael (2004)’s index and A-SAM ($\text{cor} = 0.0076$, $\text{p-value} = 0.87$). Thus, the tropospheric A-SAM index represents a zonal displacement in the position of the climatological wave-3 pattern.

The amplitude of the first zonal wavenumbers at each latitude at 50 hPa and 700 hPa are shown in Figure 8, where wavenumber zero represents the amplitude of the zonal mean. Zonal wave amplitudes of the spatial pattern described by the SAM index (Figure 8 column a) are dominated by the zonal mean (wavenumber 0) at both levels. However, zonal waves are important, particularly South of 50°S, with wavenumber 1 clearly dominating at 50 hPa (Figure 8a.1) and a mix of waves of similar amplitude at 700 hPa (Figure 8a.2). Figure 8 column b shows that the A-SAM is overwhelmingly dominated by wave 1 in the stratosphere (Figure 8b.1), while in the troposphere it is explained by a combination of zonal waves 3 to 1 in decreasing level of importance (Figure 8b.2) with negligible amplitude of the zonal mean. On the other hand, the S-SAM it is almost entirely explained by the zonal mean at both levels (Figure 8 column c), with little to no contribution from zonal waves with wavenumbers 1 to 3.

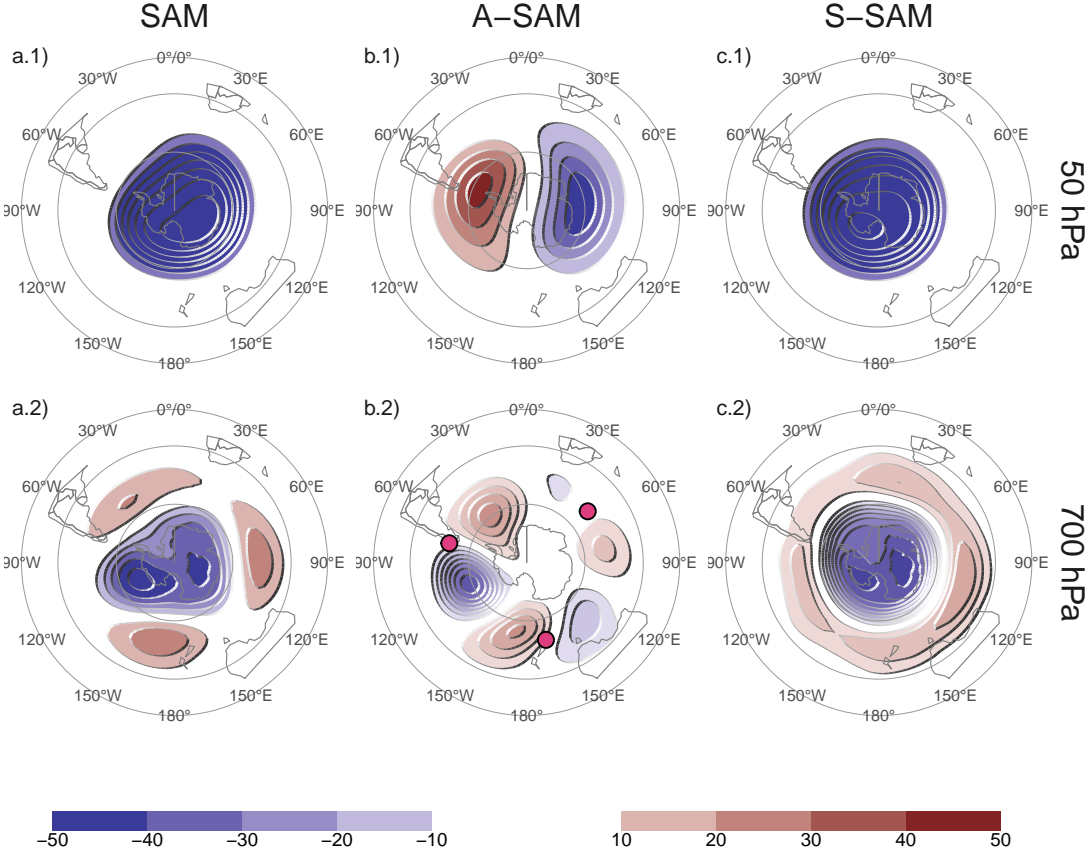


Figure 7: Regression of geopotential height (meters) at (row 1) 50 hPa and (row 2) 700 hPa with (column a) SAM, (column b) A-SAM, and (column c) S-SAM for the 1979 – 2018 period. The regression patterns for A-SAM and S-SAM are the result of one multiple regression using both indices. Points marked on panel b.2 are the location of the reference points used by Raphael (2004) for their Zonal Wave 3 index.

Looking at Figure 7b.2, it becomes apparent that zonal waves 1 and 2 modulate the amplitude of zonal wave 3, which – as mentioned before – is larger in the Western Hemisphere than in the Eastern Hemisphere.

To analyse the vertical structure of the geopotential height anomalies associated with the A-SAM index, we show a vertical cross section of regressions of mean geopotential height between 65°S and 40°S for the 50 hPa A-SAM index (Figure 9a) and for the 700 hPa A-SAM index (Figure 9b). The geopotential height anomalies associated with the stratospheric A-SAM (Figure 9a) are clearly constrained to the stratosphere, which underscores the uncoupling between the stratospheric and tropospheric A-SAM. The vertical structure of this signal tilts about 60° to the West between 100 hPa and 1 hPa, suggesting baroclinic processes. The signal in the stratosphere maximises near 10 hPa despite using the 50 hPa index for the regression.

The tropospheric A-SAM (Figure 9b) has significant signals that extend upwards to the uppermost levels considered. In the troposphere, the wave-3 structure is equivalent barotropic with maximum amplitude at roughly 250 hPa. The anomalies are larger in the Western hemisphere, where they extend into the stratosphere. In the Eastern hemisphere the wave-3 signal is smaller and confined to the troposphere while negative anomalies dominate in the stratosphere. So, while the tropospheric A-SAM index is associated with stratospheric geopotential anomalies, these do not project strongly onto the stratospheric A-SAM. The structures shown in Figure 9 are robust to the choice of index level. For any stratospheric (above 100 hPa) index, the resulting anomalies are very similar to the wave-1 structure with maximum near 10 hPa in Figure 9a. Conversely, for any tropospheric (below 100 hPa) index, the result is very similar to Figure 9b. The patterns mainly change in amplitude (not shown).

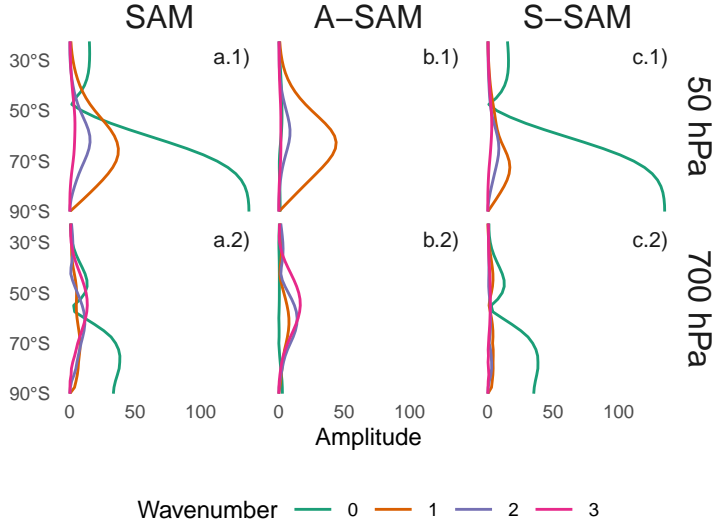


Figure 8: Amplitude (meters) of zonal waves of the geopotential height regression patterns in Figure 7 for zonal waves with wavenumber 0, 1, 2, and 3, where wavenumber 0 represents the amplitude of the zonal mean.

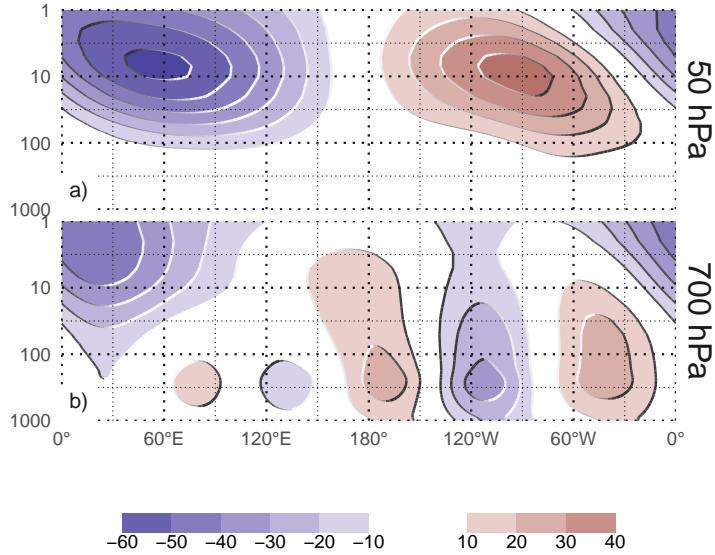


Figure 9: Regression between monthly geopotential height anomalies (meters) averaged between 65° and 40°S and the A-SAM index (extracted from a multiple regression which included the S-SAM index). (a) With the A-SAM in 50 hPa and (b) in 700 hPa for the 1979 – 2018 period.

The wave-3 pattern from Figure 7b.2 is very similar to the PSA Pattern (Mo and Ghil, 1987; Kidson, 1988) which is a teleconnection pattern associated with the ENSO (Karoly, 1989). Indeed, Fogt et al. (2011) showed that there is a significant relationship between the SAM and the ENSO. The correlation between the SAM and the ENSO as measured by the Oceanic Niño Index (ONI, Bamston et al., 1997) is -0.16 (p-value < 0.001). This relationship is captured mainly by the A-SAM, as this index has a partial correlation of -0.26 (p-value < 0.001) with the ONI, consistent with Fan (2007)’s results, whereas the S-SAM’s partial correlation with the ONI is essentially null (0.019; p-value = 0.67). The same analysis was performed using the Multivariate ENSO Index (Wolter and Timlin, 2011) and the Southern Oscillation Index (Ropelewski and Jones, 1987), obtaining similar results. The latter allows to conclude that these results do not depend on the ENSO index used.

3.3 Impacts

To assess differences in the impacts associated with the SAM, A-SAM and S-SAM indices we regressed surface land air and sea temperature and precipitation onto each of the three SAM indices at 700 hPa. As shown in previous sections, the three indices are highly coherent in the troposphere, so we select this level to represent the tropospheric circulation for consistency with previous studies.

Figure 10 shows regression coefficients of each index at 700 hPa with surface land air and sea temperature for each trimester. In Summer, positive values of the SAM index (Figure 10a.1) are associated with negative temperature anomalies near Antarctica which are surrounded by a ring of positive anomalies. The ring is not zonally symmetric, as there are four distinctive local maximums around 30°W, 120°W, 150°E and 90°E respectively. In the tropics, there are negative anomalies in the equatorial Pacific, consistent with the negative correlation between SAM and ENSO. Figure 10b.1 and c.1 show temperature anomalies associated with positive values of A-SAM and S-SAM, respectively. Both the local maximums in the ring and the anomalies in the Pacific regions are present mostly on the A-SAM regression map, while temperature patterns linked to positive S-SAM show a more zonally consistent ring and less relation to the tropics. Temperature anomalies in the Indian ocean, South Africa and Australia are strongly related to A-SAM. This signal is not present in the regression pattern with the SAM. Spring (Figure 10, row 4) features similar patterns but of smaller magnitude, with fewer regions where regressed anomalies have statistical significance.

In Autumn and Winter (rows 2 and 3 in Figure 10) the positive ring is only present through its local maximums in the regression with the SAM. There are also negative anomalies in Southern Australia, and positive anomalies over New Zealand and Southern South America. These patterns are not significant in the sense that there are no areas with p-values below 0.05 when controlling for FDR following Wilks (2016). However, repeating this analysis with 2-meter air temperature from ERA5 resulted in similar patterns that were statistically significant (not shown). Moreover, similar features were observed in station measurements by Jones et al. (2019), although using data from 1957 to 2016.

The pattern of negative anomalies in the pole surrounded by positive anomalies roughly seen in all seasons – although with varying intensity and small-scale details – translates to enhanced meridional temperature gradient maximised in the zero line, which is consistent with the intensification and poleward migration of the westerlies commonly linked to the SAM through thermal wind balance. It’s then not surprising to see it more clearly in association with S-SAM (at least in Summer and Spring).

Figure 10 column b can be partially compared with Figure 11 from Fogt et al. (2012). Although they used station data from 1958 to 2001, main features are reproduced here, such as the strong signal in New Zealand and Australia in Summer and Spring.

Regression of the SAM indices with seasonal mean precipitation and 700 hPa geopotential height are shown in Figures 11 and 12 for New Zealand and neighbouring islands, and South America respectively. South Africa is not shown because no significant signal was detected there.

In Australia, the annual regression shows that the SAM index is associated with positive precipitation anomalies in the Southeastern region (Figure 11a.1), in agreement with Gillett et al. (2006). The separation between A-SAM and S-SAM suggest that this positive anomaly is explained by the S-SAM only in the East coast (Figure 11c.1). Geopotential height anomalies associated with this index (black contours) are indicative of easterly flow from the Tasman Sea, which could explain the positive anomalies in precipitation as found by Hendon et al. (2007). A-SAM appears related to positive precipitation anomalies in the West coast of Southeastern Australia (Figure 11b.2), which could similarly be explained by the anomalous westerly circulation transporting moist air to the continent from the Indian Ocean.

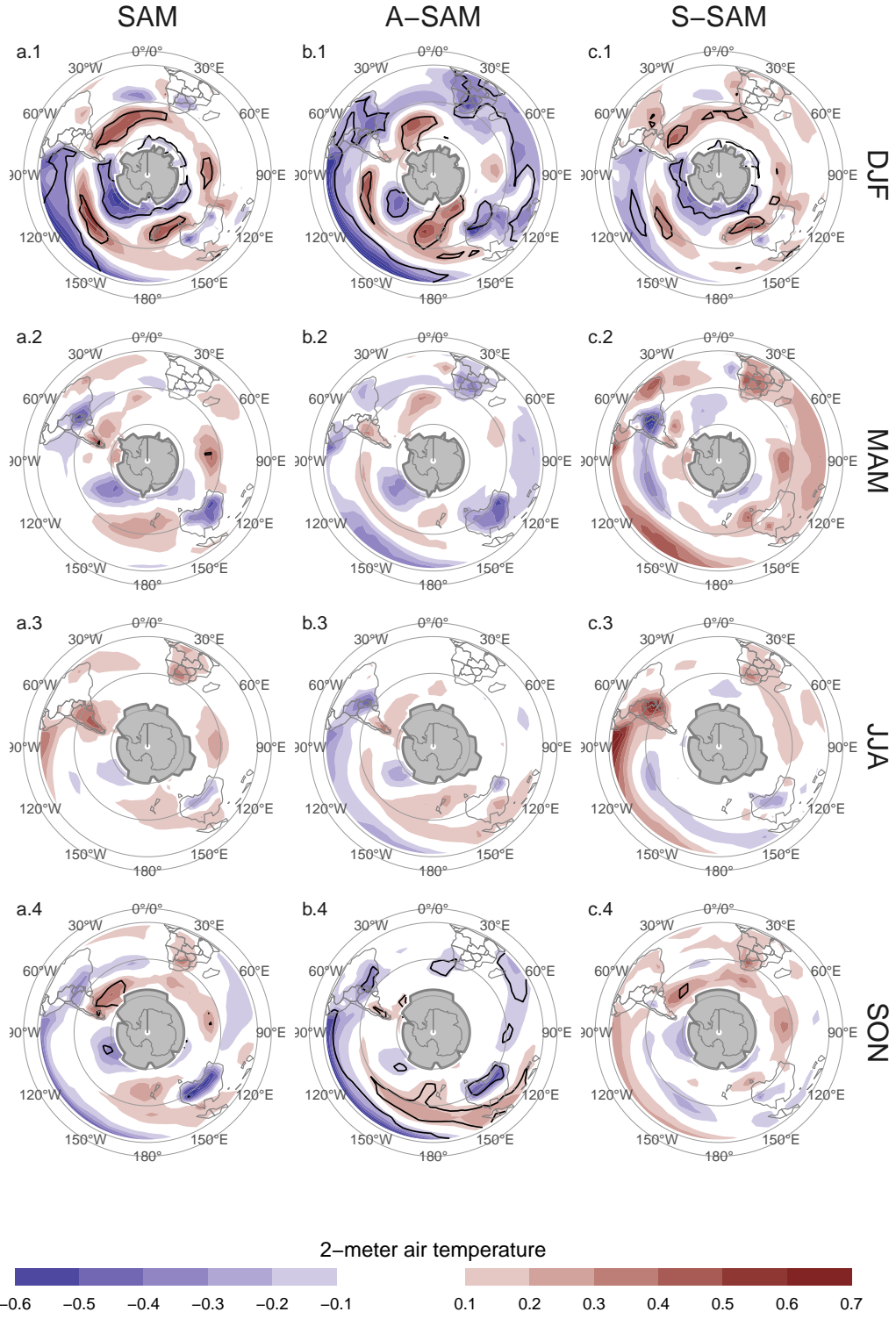


Figure 10: Regression of seasonal mean surface land air and sea temperature anomalies (Kelvin) with SAM, A-SAM and S-SAM for the 1979 – 2018 period. Black contours indicate areas with p-value smaller than 0.05 controlling for False Detection Rate. Gray areas in Antarctica have more than 15% of missing data.

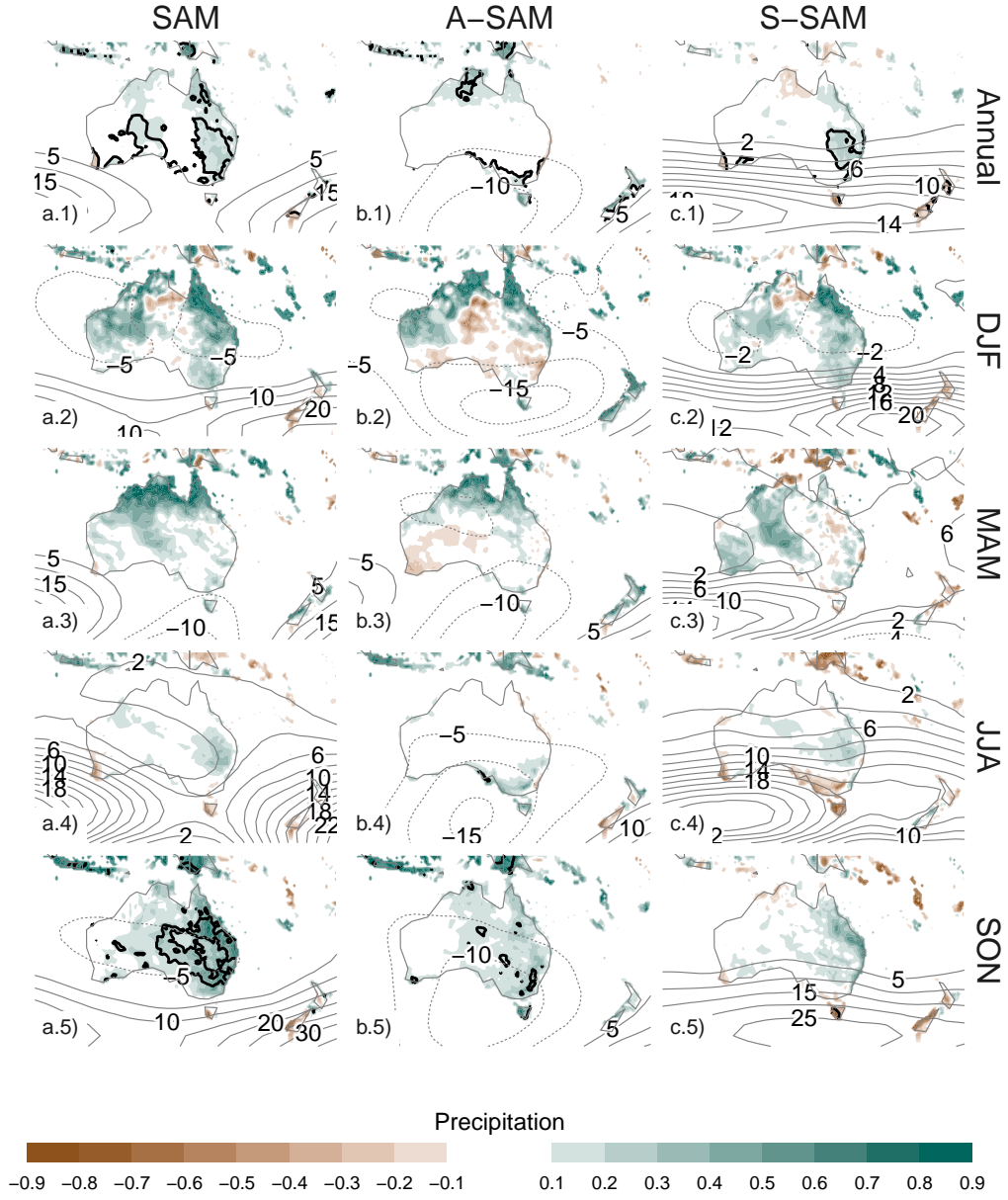


Figure 11: Regression of (row 1) annual and (rows 2 to 5) seasonal mean precipitation anomalies (mm per day, shading) and 700 hPa geopotential height anomalies (thin lines, positive values as solid lines and negative values as dashed lines) with (column a) SAM, (column (b) A-SAM and (column c) S-SAM for the 1979 – 2018 period. Thin lines are the Black contours indicate areas with p-value smaller than 0.05 controlling for False Detection Rate.

The seasonal-based regressions show statistically significant anomalies only in Spring, when positive SAM is associated with positive precipitation anomalies in Eastern Australia (Figure 11a.5). In this trimester, S-SAM seems to be associated with positive precipitation anomalies in a relatively reduced area of the East Coast (Figure 11c.5) while the positive precipitation anomalies related with positive A-SAM affect all Eastern Australia (Figure 11b.5).

In Summer, positive SAM index is associated with positive precipitation anomalies in Western and Eastern Australia, particularly in the North East (Figure 11a.2). The Eastern part being dominated by the relationship with S-SAM and the Western, by A-SAM. In Autumn, the regression with SAM shows positive anomalies in the North, similar to Summer, and a broad area of positive anomalies in the North-East to South-West direction. This structure seems to be associated with the S-SAM, while the Northern positive values are associated with the A-SAM. In Winter we see the same NE to SW aligned anomaly (although with much reduced amplitude) that is also present only in relation with the S-SAM. None of these regression coefficients are statistically significant at the 95% level. The Spring signal is broadly consistent with Hendon et al. (2007), but whereas they also detected a strong signal in Summer, Figure 11a.2 shows no statistically significant association (although the coefficients have the consistent sign).

In South America (Figure 12), regression using all seasons shows that positive SAM is associated with statistically significant negative precipitation anomalies in Southeastern South America (SESA) and Southern Chile, and non-significant positive anomalies in South Brazil, near the South Atlantic Convergence Zone (SACZ) (Figure 12a.1). Figure 12b.1 and c.1 show that while the signal over SESA and southern Brazil is associated with A-SAM, that in southern Chile is related to S-SAM.

Except Winter, seasonal-based regressions mirror this same pattern. Even if not statistically significant, they all show negative values in SESA and southern Chile along with positive values in southern Brazil in relation with the SAM. The separation of these features between A-SAM and S-SAM regression maps is also rather consistent.

The anomalous circulation at 700 hPa associated with S-SAM (Figure 12c.1) indicate anomalous easterly flow over Southern Chile. This leads to reduced influx of moist air from the Pacific Ocean which is the main source of precipitable water in that region (e.g. Garreaud, 2007). On the other hand, the anomalous circulation associated with positive values of A-SAM (Figure 12b.1) in the Atlantic is anticyclonic in the South and cyclonic in the North. This promotes anomalous South-Easterly flow over SESA, which inhibits the flow of the South America Low-Level Jet to the region (Silvestri and Vera, 2009; Zamboni et al., 2010). This same pattern was found to be associated with increased precipitation in Southern Brazil during SACZ events (Rosso et al., 2018). There is a small area of significant positive precipitation anomalies with the SAM near central Argentina which is also present in the station-based analysis by Gillett et al. (2006) that is explained by the A-SAM.

3.4 Conclusions

In this study we characterise the temporal and spatial variability of the zonally symmetric and asymmetric structure of the SAM. By projecting monthly geopotential fields at each level with the corresponding asymmetric and symmetric pattern, we created two indices for representing the zonally asymmetric and symmetric contributions of the SAM respectively.

The A-SAM index correlates strongly with the S-SAM index. In the troposphere, this correlation is maximum at zero lag, while in the stratosphere is maximised with the A-SAM leading the S-SAM by one month. Since most indices of the SAM are calculated using surface or near-surface conditions, this result would suggest that they might not be sensitive to the most dramatic changes in SAM variability.

The two-year periodicity we found in the stratospheric S-SAM might point to a link between the SAM and the Quasi Biennial Oscillation. There is evidence of influence between the QBO and the Northern Annular Mode (e.g. Holton and Tan, 1980; Watson and Gray, 2014; Zhang et al., 2020), so it is not unlikely that the SAM would be similarly affected. However, establishing this link would require further research.

We observe a positive trend of SAM in Summer and Autumn, as was documented by previous studies (e.g. Fogt and Marshall, 2020, and references therein) for low levels. We show that these trends maximise at 100 hPa, and are explained by the zonally symmetric component. We also find a statistically significant positive trend in the Symmetric component of the SAM in the stratosphere that is not evident in the SAM index. We find some evidence of the SAM becoming more zonally asymmetric, as there is a slight positive trend in the variance explained by the as the A-SAM. This is in contrast to Fogt et al. (2012) who made the

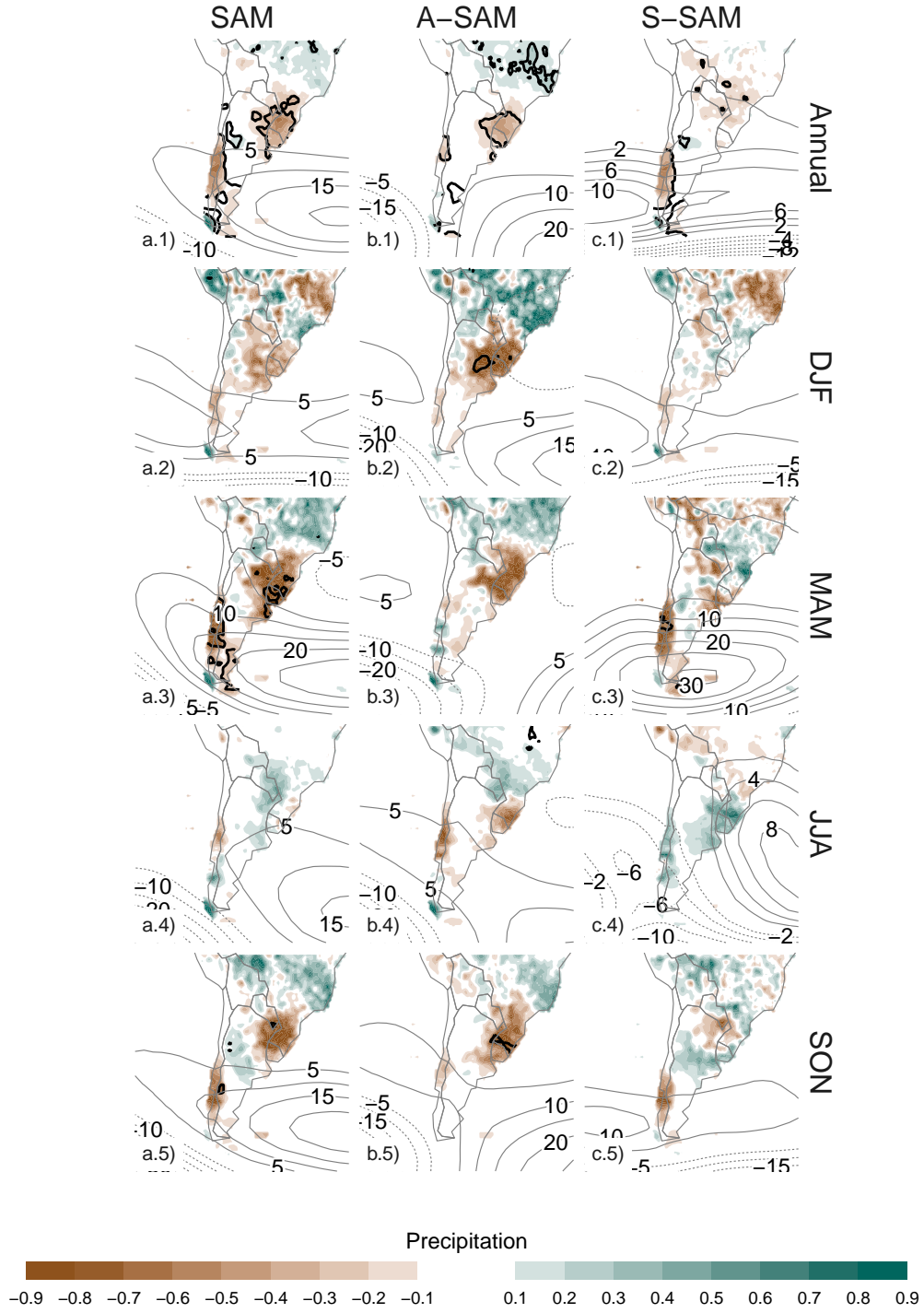


Figure 12: Same as Figure 11 but for South America.

evaluation for the period 1958 – 2001. This discrepancy might be due either due to differences in methodology or analysed period.

In the troposphere, the spatial patterns of geopotential associated with the S-SAM index are much closer to being fully annular than the patterns associated with the SAM index. The A-SAM index, on the other hand, describes a wave-3 pattern with maximum amplitude in the Pacific. This pattern extends vertically in the troposphere but its maximum is located at 250 hPa, which also could suggest that surface-based indices are not optimal for capturing this variability. This wave-3 pattern is similar to the Pacific-South American Pattern, linked to ENSO variability. We found that the significant correlation that exists between the SAM index and the Oceanic Niño Index over this period is captured entirely by the A-SAM index. This suggests that ENSO is linked to SAM exclusively through the variability in the latter’s asymmetric component and thus, the A-SAM index could be a useful measure to further study that relationship.

Temperature anomalies associated with the SAM broadly show a pattern of negative anomalies at polar latitudes surrounded by positive anomalies, but with many deviations from symmetry. The A-SAM index explains a big portion of these deviations. In particular, the positive phase of A-SAM is associated with colder temperatures over Southern Brazil, South Africa and Southern Australia, as well as the negative anomalies in the equatorial Pacific consistent with the ENSO-SAM relationship. These negative anomalies are particularly clear in the DJF and SON trimesters, which include the months in which the ENSO teleconnection is more active (e.g. Cai et al., 2020).

In Australia the SAM is associated with positive precipitation anomalies in South East and this is explained by the S-SAM. However, the A-SAM is associated with a small area of positive precipitation anomalies in the Eastern Coast of West Australia, maybe due to advection of moist air from the Indian Ocean. In South America, precipitation anomalies associated with the SAM are negative both in Southern Chile and Southeastern South America, and positive in Southern Brazil. These features are cleanly separated between A-SAM and S-SAM. S-SAM explains the negative anomalies in Southern Chile and A-SAM, the negative-positive dipole between Southeastern South America and Southern Brazil. Individual seasons mostly follow this pattern.

Silvestri and Vera (2009) suggests that precipitation impacts linked to the SAM changed strongly before and after 1980. In particular, the negative relationship with precipitation in South America was absent in some areas and switched sign in others in the earlier period. The correlation between ENSO and SAM is similarly non-stationary, also changing sign before the 1980s (Fogt and Bromwich, 2006; Clem and Fogt, 2013). Seeing as both the ENSO-SAM relationship and most of the precipitation impacts in South America are captured by the A-SAM, the results presented here are most likely period-dependent. The decadal variations of the A-SAM should be focus of future studies.

By separating the zonally symmetric and zonally asymmetric SAM signals, we show that the asymmetric component of the SAM has its unique variability, trends and impacts. This is particularly important in the context of a changing climate, as the impact on the SAM of ozone recovery is modelled as highly zonally symmetric, while the impact of increased concentration of greenhouse gases has also a zonally asymmetric component (Arblaster and Meehl, 2006).

Acknowledgements

NOAA Global Surface Temperature (NOAAGlobalTemp) data provided by the NOAA/OAR/ESRL PSL, Boulder, Colorado, USA, from their Web site at <https://psl.noaa.gov/>

Declarations

Funding

The research was supported by UBACyT20020170100428BA and the CLIMAX Project funded by Belmont Forum/ANR-15-JCL/-0002-01. Elio Campitelli was supported by a PhD grant from CONICET, Argentina.

Conflicts of interest

The authors declare that they have no conflict of interest.

Availability of data and material

All data used in this paper is freely available from their respective sources. ERA5 data can be obtained via the Copernicus Climate Data Store (<https://cds.climate.copernicus.eu/cdsapp#!/dataset/reanalysis-era5-pressure-levels-monthly-means>). NOAA GlobalTemp and GPCC precipitation data can be obtained through the NOAA Physical Sciences Laboratory website (<https://psl.noaa.gov/data/gridded/data.noaaglobaltemp.html> and <https://psl.noaa.gov/data/gridded/data.gpcc.html>). The Oceanic Niño Index is available via NOAA's Climate Prediction Center: https://www.cpc.ncep.noaa.gov/products/analysis_monitoring/ensostuff/detrend.nino34.ascii.txt

Code availability

A version-controlled repository of the code used to create this analysis, including the code used to download the data can be found at <https://github.com/eliocamp/asymsam>.

A Extra figures

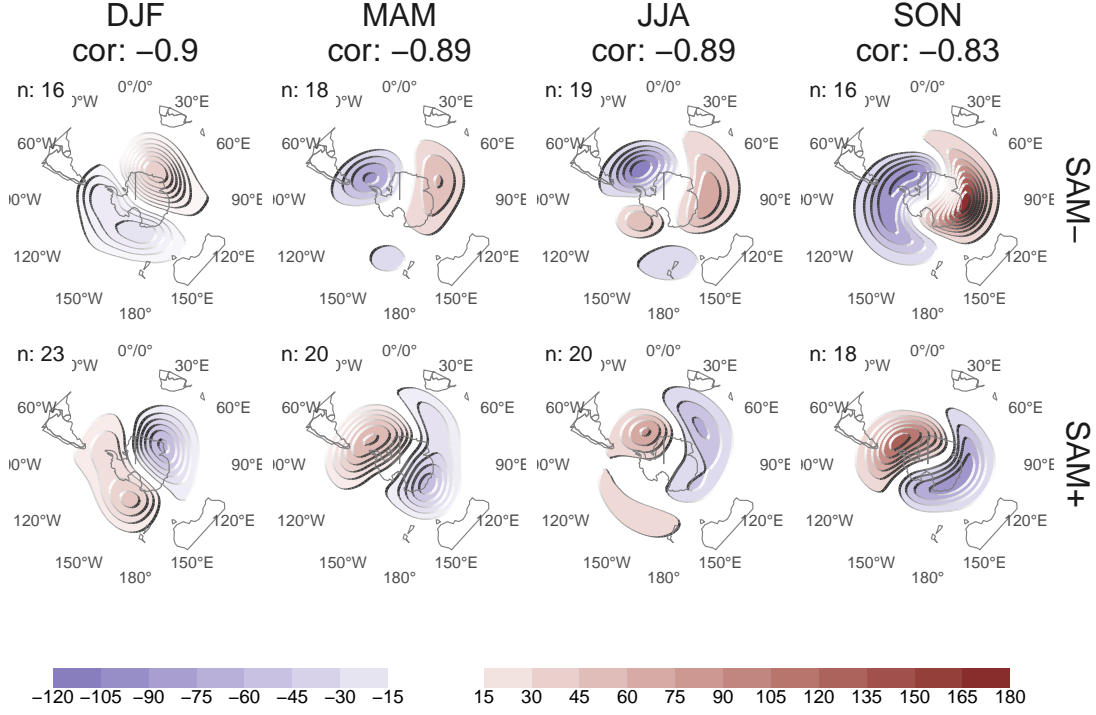


Figure A.1: 50 hPa geopotential height zonal anomalies (meters) of composites of positive and negative SAM months selected using ± 1 standard deviation as threshold for the 1979 – 2018 period. Numbers in the column headers are the spatial correlation between SAM+ and SAM- composites and number of monthly fields used to construct each composite.

References

- Sam Albers and Elio Campitelli. Rsoi: Import Various Northern and Southern Hemisphere Climate Indices, August 2020.
- JJ Allaire, Jeffrey Horner, Yihui Xie, Vicent Marti, and Natacha Porte. *Markdown: Render Markdown with the c Library 'Sundown'*, 2019.
- Julie M. Arblaster and Gerald A. Meehl. Contributions of External Forcings to Southern Annular Mode Trends. *J. Climate*, 19(12):2896–2905, June 2006. ISSN 0894-8755. doi: 10.1175/JCLI3774.1.
- M. P. Baldwin, L. J. Gray, T. J. Dunkerton, K. Hamilton, P. H. Haynes, W. J. Randel, J. R. Holton, M. J. Alexander, I. Hirota, T. Horinouchi, D. B. A. Jones, J. S. Kinnersley, C. Marquardt, K. Sato, and M. Takahashi. The quasi-biennial oscillation. *Reviews of Geophysics*, 39(2):179–229, 2001. ISSN 1944-9208. doi: 10.1029/1999RG000073.
- Mark P. Baldwin. Annular modes in global daily surface pressure. *Geophysical Research Letters*, 28(21): 4115–4118, 2001. ISSN 1944-8007. doi: 10.1029/2001GL013564.
- Mark P. Baldwin and Timothy J. Dunkerton. Stratospheric Harbingers of Anomalous Weather Regimes. *Science*, 294(5542):581–584, October 2001. ISSN 0036-8075, 1095-9203. doi: 10.1126/science.1063315.

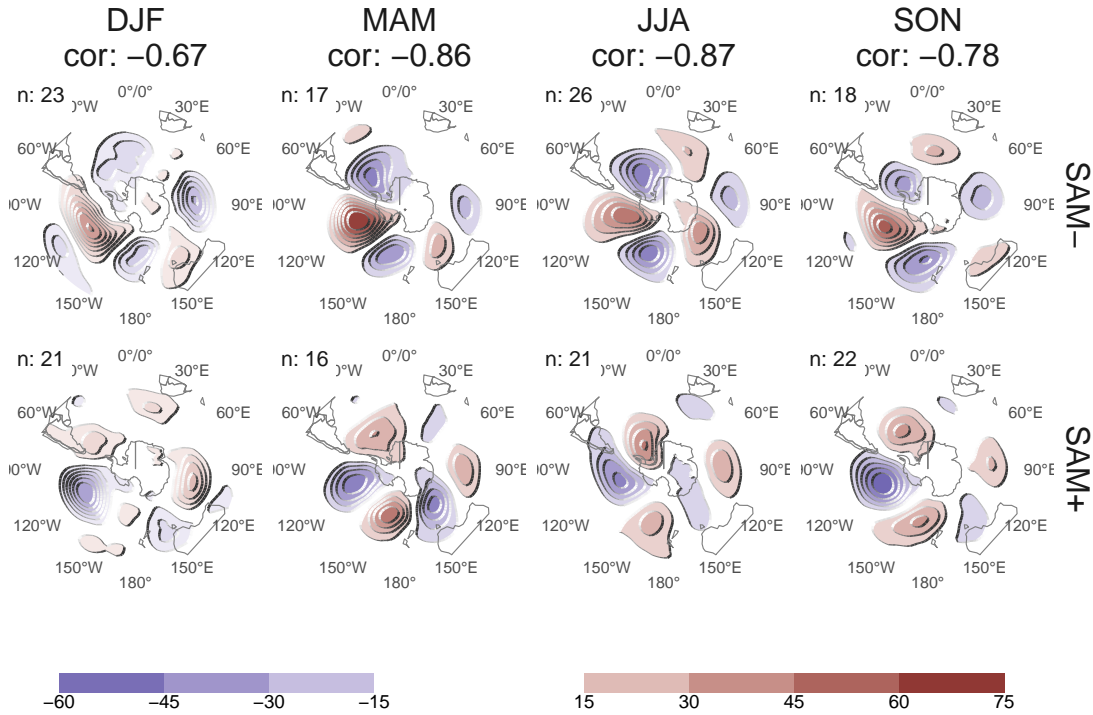


Figure A.2: Same as A.1 but for 700 hPa geopotential height.

- Mark P. Baldwin and David W. J. Thompson. A critical comparison of stratosphere–troposphere coupling indices. *Quarterly Journal of the Royal Meteorological Society*, 135(644):1661–1672, 2009. ISSN 1477-870X. doi: 10.1002/qj.479.
- Anthony G. Bamston, Muthuvel Chelliah, and Stanley B. Goldenberg. Documentation of a highly ENSO-related sst region in the equatorial pacific: Research note. *Atmosphere-Ocean*, 35(3):367–383, September 1997. ISSN 0705-5900. doi: 10.1080/07055900.1997.9649597.
- Yoav Benjamini and Yosef Hochberg. Controlling the False Discovery Rate: A Practical and Powerful Approach to Multiple Testing. *Journal of the Royal Statistical Society: Series B (Methodological)*, 57(1): 289–300, 1995. ISSN 2517-6161. doi: 10.1111/j.2517-6161.1995.tb02031.x.
- Wenju Cai, Michael J. McPhaden, Alice M. Grimm, Regina R. Rodrigues, Andréa S. Taschetto, René D. Garreaud, Boris Dewitte, Germán Poveda, Yoo-Geun Ham, Agus Santoso, Benjamin Ng, Weston Anderson, Guojian Wang, Tao Geng, Hyun-Su Jo, José A. Marengo, Lincoln M. Alves, Marisol Osman, Shujun Li, Lixin Wu, Christina Karamperidou, Ken Takahashi, and Carolina Vera. Climate impacts of the El Niño–Southern Oscillation on South America. *Nature Reviews Earth & Environment*, 1(4):215–231, April 2020. ISSN 2662-138X. doi: 10.1038/s43017-020-0040-3.
- Elio Campitelli. metR: Tools for Easier Analysis of Meteorological Fields, April 2020.
- Chul Chung and Sumant Nigam. Weighting of geophysical data in Principal Component Analysis. *Journal of Geophysical Research: Atmospheres*, 104(D14):16925–16928, 1999. ISSN 2156-2202. doi: 10.1029/1999JD900234.
- Kyle R. Clem and Ryan L. Fogt. Varying roles of ENSO and SAM on the Antarctic Peninsula climate in austral spring. *Journal of Geophysical Research: Atmospheres*, 118(20):11,481–11,492, 2013. ISSN 2169-8996. doi: 10.1002/jgrd.50860.
- Matt Dowle, Arun Srinivasan, Jan Gorecki, Michael Chirico, Pasha Stetsenko, Tom Short, Steve Lianoglou, Eduard Antonyan, Markus Bonsch, Hugh Parsonage, Scott Ritchie, Kun Ren, Xianying Tan, Rick Saporta,

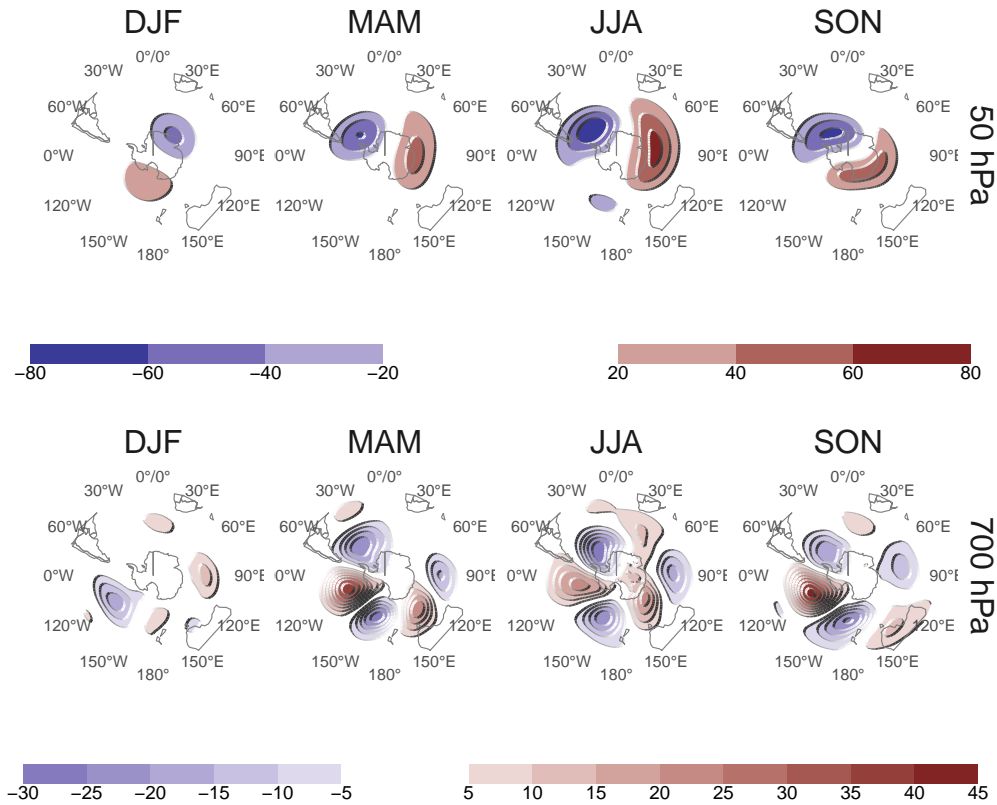


Figure A.3: Regression coefficients of 50 hPa and 700 hPa geopotential height zonal anomalies (meters) onto the standardised timeseries of the leading EOF computed for each season independently for the 1979 – 2018 period.

Otto Seiskari, Xianghui Dong, Michel Lang, Watal Iwasaki, Seth Wenchel, Karl Broman, Tobias Schmidt, David Arenburg, Ethan Smith, Francois Cocquemas, Matthieu Gomez, Philippe Chataignon, Nello Blaser, Dmitry Selivanov, Andrey Riabushenko, Cheng Lee, Declan Groves, Daniel Possenriede, Felipe Parages, Denes Toth, Mus Yaramaz-David, Ayappan Perumal, James Sams, Martin Morgan, Michael Quinn, @javrucebo, @marc-outines, Roy Storey, Manish Saraswat, Morgan Jacob, Michael Schubmehl, Davis Vaughan, Toby Hocking, Leonardo Silvestri, Tyson Barrett, Jim Hester, Anthony Damico, Sebastian Freundt, David Simons, Elliott Sales de Andrade, Cole Miller, Jens Peder Meldgaard, Vaclav Tlapak, and Kevin Ushey. Data.table: Extension of 'data.frame', July 2020.

Ke Fan. Zonal asymmetry of the Antarctic Oscillation. *Geophysical Research Letters*, 34(2), January 2007. ISSN 0094-8276. doi: 10.1029/2006GL028045.

Ryan L. Fogt and David H. Bromwich. Decadal Variability of the ENSO Teleconnection to the High-Latitude South Pacific Governed by Coupling with the Southern Annular Mode. *J. Climate*, 19(6):979–997, March 2006. ISSN 0894-8755. doi: 10.1175/JCLI3671.1.

Ryan L. Fogt and Gareth J. Marshall. The Southern Annular Mode: Variability, trends, and climate impacts across the Southern Hemisphere. *WIREs Climate Change*, 11(4):e652, 2020. ISSN 1757-7799. doi: 10.1002/wcc.652.

Ryan L. Fogt, David H. Bromwich, and Keith M. Hines. Understanding the SAM influence on the South Pacific ENSO teleconnection. *Clim Dyn*, 36(7):1555–1576, April 2011. ISSN 1432-0894. doi: 10.1007/s00382-010-0905-0.

Ryan L. Fogt, Julie M. Jones, and James Renwick. Seasonal Zonal Asymmetries in the Southern Annular Mode and Their Impact on Regional Temperature Anomalies. *J. Climate*, 25(18):6253–6270, April 2012. ISSN 0894-8755. doi: 10.1175/JCLI-D-11-00474.1.

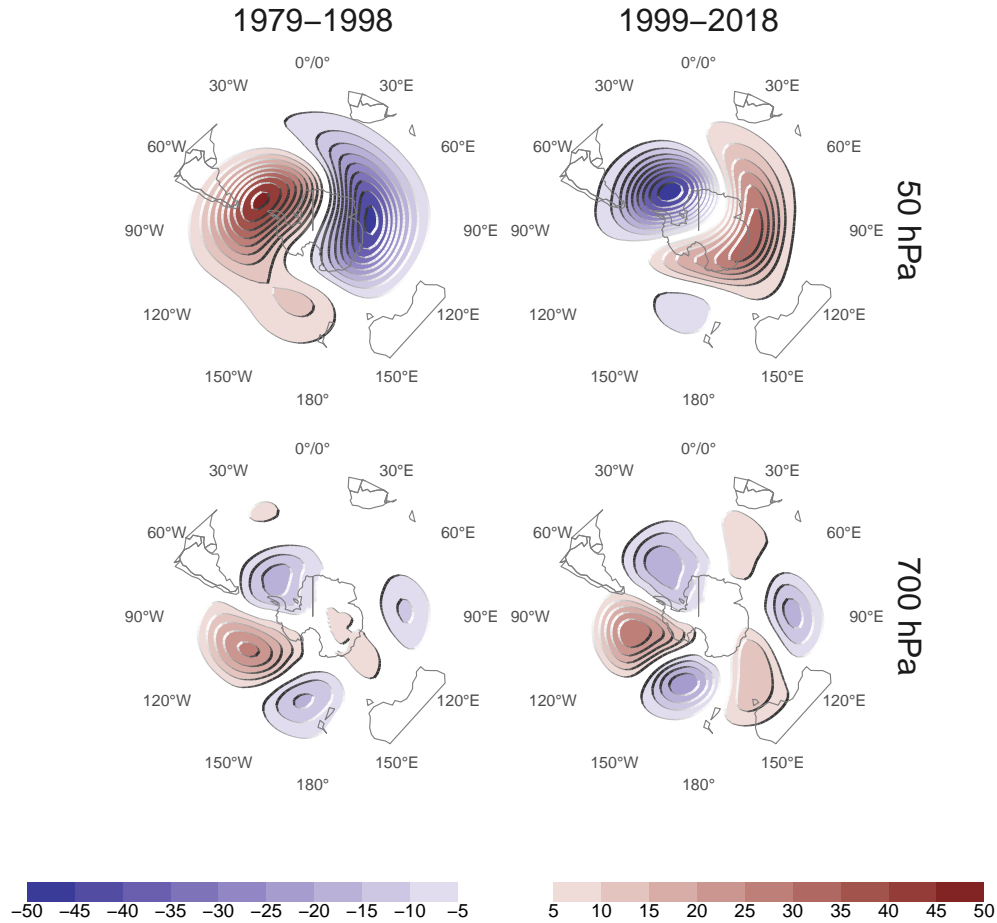


Figure A.4: Regression of 50 hPa and 700 hPa geopotential height zonal anomalies (meters) onto the standardised timeseries of the leading EOF computed for the periods 1979 – 1998 and 1999 – 2018. Spatial correlation between both fields is 0.86 for the 50 hPa fields and 0.76 for the 700 hPa fields.

RenéD Garreaud. Precipitation and Circulation Covariability in the Extratropics. *J. Climate*, 20(18):4789–4797, September 2007. ISSN 0894-8755. doi: 10.1175/JCLI4257.1.

N. P. Gillett, R. J. Allan, and T. J. Ansell. Detection of external influence on sea level pressure with a multi-model ensemble. *Geophysical Research Letters*, 32(19), 2005. ISSN 1944-8007. doi: 10.1029/2005GL023640.

N. P. Gillett, T. D. Kell, and P. D. Jones. Regional climate impacts of the Southern Annular Mode. *Geophysical Research Letters*, 33(23), 2006. ISSN 1944-8007. doi: 10.1029/2006GL027721.

Nathan P. Gillett, John C. Fyfe, and David E. Parker. Attribution of observed sea level pressure trends to greenhouse gas, aerosol, and ozone changes. *Geophysical Research Letters*, 40(10):2302–2306, 2013. ISSN 1944-8007. doi: 10.1002/grl.50500.

Daoyi Gong and Shaowu Wang. Definition of Antarctic Oscillation index. *Geophysical Research Letters*, 26(4):459–462, 1999. ISSN 1944-8007. doi: 10.1029/1999GL900003.

Harry H. Hendon, David W. J. Thompson, and Matthew C. Wheeler. Australian Rainfall and Surface Temperature Variations Associated with the Southern Hemisphere Annular Mode. *J. Climate*, 20(11):2452–2467, June 2007. ISSN 0894-8755. doi: 10.1175/JCLI4134.1.

Hans Hersbach, Bill Bell, Paul Berrisford, Shoji Hirahara, András Horányi, Joaquín Muñoz-Sabater, Julien Nicolas, Carole Peubey, Raluca Radu, Dinand Schepers, Adrian Simmons, Cornel Soci, Saleh Abdalla, Xavier Abellan, Gianpaolo Balsamo, Peter Bechtold, Gionata Biavati, Jean Bidlot, Massimo Bonavita, Giovanna De Chiara, Per Dahlgren, Dick Dee, Michail Diamantakis, Rossana Dragani, Johannes Flemming, Richard Forbes, Manuel Fuentes, Alan Geer, Leo Haimberger, Sean Healy, Robin J. Hogan, Elías Hólm,

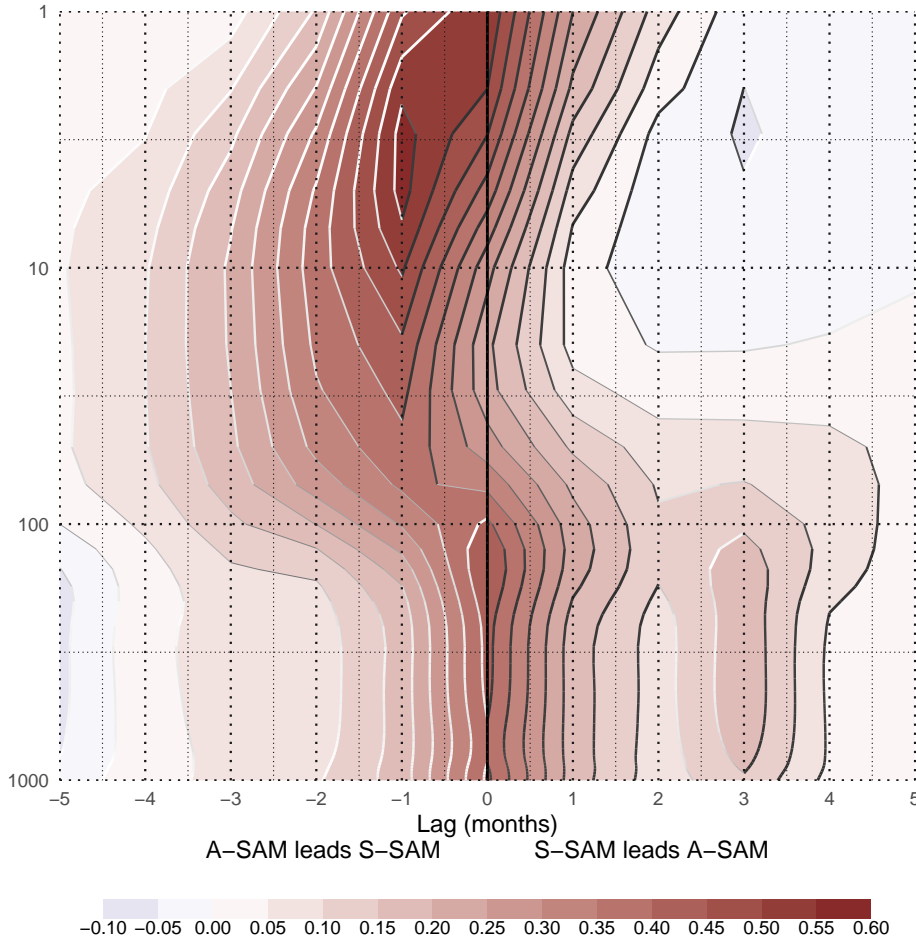


Figure A.5: Lag-correlation between the A-SAM and the S-SAM index at each level. Negative lags imply A-SAM leading S-SAM and vice versa. For the 1979 – 2018 period.

- Marta Janisková, Sarah Keeley, Patrick Laloyaux, Philippe Lopez, Cristina Lupu, Gabor Radnoti, Patricia de Rosnay, Iryna Rozum, Freja Vamborg, Sebastien Villaume, and Jean-Noël Thépaut. The ERA5 global reanalysis. *Quarterly Journal of the Royal Meteorological Society*, 146(730):1999–2049, 2020. ISSN 1477-870X. doi: 10.1002/qj.3803.
- M. Ho, A. S. Kiem, and D. C. Verdon-Kidd. The Southern Annular Mode: A comparison of indices. *Hydrology and Earth System Sciences*, 16(3):967–982, March 2012. ISSN 1027-5606. doi: 10.5194/hess-16-967-2012.
- James R. Holton and Hsiu-Chi Tan. The Influence of the Equatorial Quasi-Biennial Oscillation on the Global Circulation at 50 mb. *J. Atmos. Sci.*, 37(10):2200–2208, October 1980. ISSN 0022-4928. doi: 10.1175/1520-0469(1980)037<2200:TIOTEQ>2.0.CO;2.
- Koen Hufkens, Reto Stauffer, and Elio Campitelli. Ecmwfr: Interface to 'ECMWF' and 'CDS' Data Web Services, July 2020.
- Julie M. Jones, Ryan L. Fogt, Martin Widmann, Gareth J. Marshall, Phil D. Jones, and Martin Visbeck. Historical SAM Variability. Part I: Century-Length Seasonal Reconstructions. *J. Climate*, 22(20):5319–5345, October 2009. ISSN 0894-8755. doi: 10.1175/2009JCLI2785.1.
- Megan E. Jones, David H. Bromwich, Julien P. Nicolas, Jorge Carrasco, Eva Plavcová, Xun Zou, and Sheng-Hung Wang. Sixty Years of Widespread Warming in the Southern Middle and High Latitudes (1957–2016). *J. Climate*, 32(20):6875–6898, October 2019. ISSN 0894-8755. doi: 10.1175/JCLI-D-18-0565.1.
- David J. Karoly. Southern Hemisphere Circulation Features Associated with El Niño-Southern Oscillation Events. *J. Climate*, 2(11):1239–1252, November 1989. ISSN 0894-8755. doi: 10.1175/1520-0442(1989)002<1239:SHCFW>2.0.CO;2.

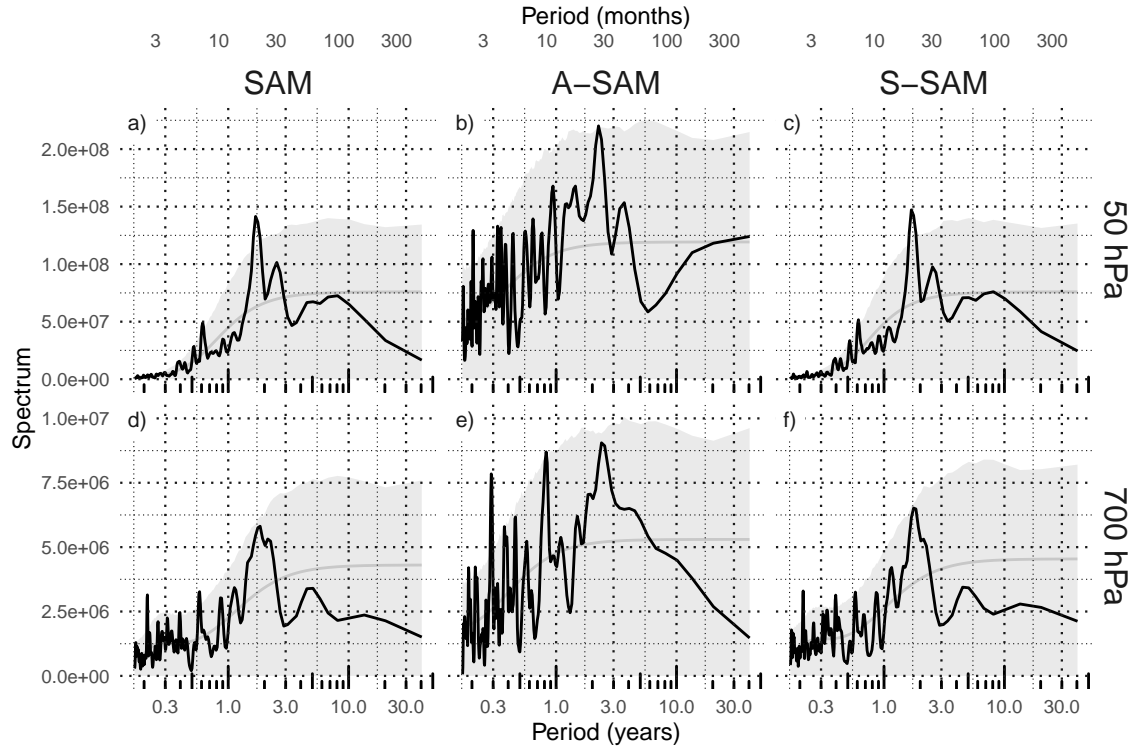


Figure A.6: Fourier spectrum of each timeseries computed as Fourier transform smoothed with modified Daniell smoothers with widths 3 and 5. The shading indicates the 95% confidence area derived by computing the spectrum for 5000 simulated samples from a fitted autoregressive model and (95% of the simulated samples had an amplitude equal or lower). The light line indicates the theoretical expected amplitude from the autoregressive model. For the 1979 – 2018 period.

- Richard W. Katz and Barbara G. Brown. The problem of multiplicity in research on teleconnections. *International Journal of Climatology*, 11(5):505–513, 1991. ISSN 1097-0088. doi: 10.1002/joc.3370110504.
- John W. Kidson. Interannual Variations in the Southern Hemisphere Circulation. *J. Climate*, 1(12):1177–1198, December 1988. ISSN 0894-8755. doi: 10.1175/1520-0442(1988)001<1177:IVITSH>2.0.CO;2.
- Eun-Pa Lim, Harry H. Hendon, Julie M. Arblaster, Francois Delage, Hanh Nguyen, Seung-Ki Min, and Matthew C. Wheeler. The impact of the Southern Annular Mode on future changes in Southern Hemisphere rainfall. *Geophysical Research Letters*, 43(13):7160–7167, 2016. ISSN 1944-8007. doi: 10.1002/2016GL069453.
- Gareth J. Marshall. Trends in the Southern Annular Mode from Observations and Reanalyses. *J. Climate*, 16(24):4134–4143, December 2003. ISSN 0894-8755. doi: 10.1175/1520-0442(2003)016<4134:TITSAM>2.0.CO;2.
- Gareth J. Marshall, Peter A. Stott, John Turner, William M. Connolley, John C. King, and Thomas A. Lachlan-Cope. Causes of exceptional atmospheric circulation changes in the Southern Hemisphere. *Geophysical Research Letters*, 31(14), 2004. ISSN 1944-8007. doi: 10.1029/2004GL019952.
- Kingtse C. Mo and Michael Ghil. Statistics and Dynamics of Persistent Anomalies. *J. Atmos. Sci.*, 44(5): 877–902, March 1987. ISSN 0022-4928. doi: 10.1175/1520-0469(1987)044<0877:SADOPA>2.0.CO;2.
- R Core Team. *R: A Language and Environment for Statistical Computing*. R Foundation for Statistical Computing, Vienna, Austria, 2020.
- M. N. Raphael. A zonal wave 3 index for the Southern Hemisphere. *Geophysical Research Letters*, 31(23), 2004. ISSN 1944-8007. doi: 10.1029/2004GL020365.
- Jeffery C. Rogers and Harry van Loon. Spatial Variability of Sea Level Pressure and 500 mb Height Anomalies over the Southern Hemisphere. *Mon. Wea. Rev.*, 110(10):1375–1392, October 1982. ISSN 0027-0644. doi: 10.1175/1520-0493(1982)110<1375:SVOSLP>2.0.CO;2.

- C. F. Ropelewski and P. D. Jones. An Extension of the Tahiti–Darwin Southern Oscillation Index. *Mon. Wea. Rev.*, 115(9):2161–2165, September 1987. ISSN 0027-0644. doi: 10.1175/1520-0493(1987)115<2161:AEOTTS>2.0.CO;2.
- Flávia Venturini Rosso, Nathalie Tissot Boiaski, Simone Erotildes Teleginski Ferraz, and Tiago Capello Robles. Influence of the Antarctic Oscillation on the South Atlantic Convergence Zone. *Atmosphere*, 9(11):431, November 2018. doi: 10.3390/atmos9110431.
- Udo Schneider, Andreas Becker, Peter Finger, Anja Meyer-Christoffer, Bruno Rudolf, and Markus Ziese. GPCC Full Data Reanalysis Version 7.0 at 0.5°: Monthly Land-Surface Precipitation from Rain-Gauges built on GTS-based and Historic Data: Gridded Monthly Totals, 2015.
- Udo Schneider, Peter Finger, Anja Meyer-Christoffer, Elke Rustemeier, Markus Ziese, and Andreas Becker. Evaluating the Hydrological Cycle over Land Using the Newly-Corrected Precipitation Climatology from the Global Precipitation Climatology Centre (GPCC). *Atmosphere*, 8(3):52, March 2017. doi: 10.3390/atmos8030052.
- S. J. Sheather and M. C. Jones. A Reliable Data-Based Bandwidth Selection Method for Kernel Density Estimation. *Journal of the Royal Statistical Society. Series B (Methodological)*, 53(3):683–690, 1991. ISSN 0035-9246.
- Gabriel Silvestri and Carolina Vera. Nonstationary Impacts of the Southern Annular Mode on Southern Hemisphere Climate. *J. Climate*, 22(22):6142–6148, November 2009. ISSN 0894-8755. doi: 10.1175/2009JCLI3036.1.
- Thomas M. Smith, Richard W. Reynolds, Thomas C. Peterson, and Jay Lawrimore. Improvements to NOAA’s Historical Merged Land–Ocean Surface Temperature Analysis (1880–2006). *J. Climate*, 21(10):2283–2296, May 2008. ISSN 0894-8755. doi: 10.1175/2007JCLI2100.1.
- Russell S. Vose, Derek Arndt, Viva F. Banzon, David R. Easterling, Byron Gleason, Boyin Huang, Ed Kearns, Jay H. Lawrimore, Matthew J. Menne, Thomas C. Peterson, Richard W. Reynolds, Thomas M. Smith, Claude N. Williams, and David B. Wuertz. NOAA’s Merged Land–Ocean Surface Temperature Analysis. *Bull. Amer. Meteor. Soc.*, 93(11):1677–1685, November 2012. ISSN 0003-0007. doi: 10.1175/BAMS-D-11-00241.1.
- Sir Gilbert Thomas Walker. *Correlation in Seasonal Variations of Weather, III: On the Criterion for the Reality of Relationships Or Periodicities*. Meteorological Office, 1914.
- Peter A. G. Watson and Lesley J. Gray. How Does the Quasi-Biennial Oscillation Affect the Stratospheric Polar Vortex? *J. Atmos. Sci.*, 71(1):391–409, January 2014. ISSN 0022-4928. doi: 10.1175/JAS-D-13-096.1.
- Hadley Wickham. *Ggplot2: Elegant Graphics for Data Analysis*. Use R! Springer-Verlag, New York, 2009. ISBN 978-0-387-98141-3. doi: 10.1007/978-0-387-98141-3.
- D. S. Wilks. “The Stippling Shows Statistically Significant Grid Points”: How Research Results are Routinely Overstated and Overinterpreted, and What to Do about It. *Bull. Amer. Meteor. Soc.*, 97(12):2263–2273, March 2016. ISSN 0003-0007. doi: 10.1175/BAMS-D-15-00267.1.
- Klaus Wolter and Michael S. Timlin. El Niño/Southern Oscillation behaviour since 1871 as diagnosed in an extended multivariate ENSO index (MEI.ext). *International Journal of Climatology*, 31(7):1074–1087, 2011. ISSN 1097-0088. doi: 10.1002/joc.2336.
- Yihui Xie. *Dynamic Documents with R and Knitr*. Chapman and Hall/CRC, Boca Raton, Florida, second edition, 2015.
- Laura Zamboni, Carlos R. Mechoso, and Fred Kucharski. Relationships between Upper-Level Circulation over South America and Rainfall over Southeastern South America: A Physical Base for Seasonal Predictions. *J. Climate*, 23(12):3300–3315, June 2010. ISSN 0894-8755. doi: 10.1175/2009JCLI3129.1.
- Ruhua Zhang, Wenshou Tian, and Tao Wang. Role of the quasi-biennial oscillation in the downward extension of stratospheric northern annular mode anomalies. *Clim Dyn*, 55(3):595–612, August 2020. ISSN 1432-0894. doi: 10.1007/s00382-020-05285-4.